Design and Characterization of Innovative Gas-Atomized Al-Si-Cu-Mg Alloys for Additive Manufacturing

metals

MDPI

Article

Design and Characterization of Innovative Gas-Atomized Al-Si-Cu-Mg Alloys for Additive Manufacturing

Matteo Vanzetti [1,2,*], Michael J. Pavel [3], C. Jacob Williamson [3], Elisa Padovano [1], Lorena I. Pérez-Andrade [3], Mark Weaver [3], Luke N. Brewer [3], Federica Bondioli [1,4] and Paolo Fino [1]

[1] Department of Applied Science and Technology, Politecnico di Torino, Corso Duca degli Abruzzi 24, 10129 Torino, Italy; elisa.padovano@polito.it (E.P.); federica.bondioli@polito.it (F.B.); paolo.fino@polito.it (P.F.)
[2] Center for Sustainable Future Technologies IIT@Polito, Istituto Italiano di Tecnologia, Via Livorno 60, 10124 Torino, Italy
[3] Department of Mechanical Engineering, The University of Alabama, Tuscaloosa, AL 35401, USA; mjpavel@crimson.ua.edu (M.J.P.); liperezandrade@ua.edu (L.I.P.-A.); mweaver@eng.ua.edu (M.W.); lnbrewer1@eng.ua.edu (L.N.B.)
[4] Consorzio Interuniversitario Nazionale per la Scienza e Tecnologia dei Materiali (INSTM), Via G. Giusti 9, 50121 Firenze, Italy
* Correspondence: matteo.vanzetti@polito.it

Abstract: Metallic powders are widely utilized as feedstock materials in metal additive manufacturing (MAM). However, only a limited number of alloys can currently be processed using these technologies, with most of them being casting alloys. The objective of this study is to investigate novel aluminum alloys produced via a close-coupled gas atomizer (CCGA) by adding an increasing amount of copper (4, 8, and 20 wt%) to an AlSi10Mg alloy. The obtained powders were fully characterized to evaluate the effect of copper, a well-established strengthener for aluminum alloys, in order to correlate the obtained hardness to the powder phase composition and microstructure. In particular, a dendritic microstructure was observed in all alloys, and, as the copper content was increased, the size of the secondary dendrite arm spacing (SDAS) decreased progressively. Consequently, the hardness measured on the powder cross-section linearly increased with the copper content, and the hardness value of 185 ± 13 HV of the AlCu20Si10Mg composition was found to be twice that of the AlSi10Mg alloy (88 ± 5 HV).

Keywords: additive manufacturing; powder; laser powder bed fusion; aluminum alloy; AlSi10Mg; copper; microstructure

Citation: Vanzetti, M.; Pavel, M.J.; Williamson, C.J.; Padovano, E.; Pérez-Andrade, L.I.; Weaver, M.; Brewer, L.N.; Bondioli, F.; Fino, P. Design and Characterization of Innovative Gas-Atomized Al-Si-Cu-Mg Alloys for Additive Manufacturing. *Metals* **2023**, *13*, 1845. https://doi.org/10.3390/met13111845

Academic Editor: Gang Fang

Received: 11 October 2023
Revised: 26 October 2023
Accepted: 31 October 2023
Published: 3 November 2023

1. Introduction

Metal additive manufacturing (MAM) has undergone significant advancements in recent decades, offering numerous advantages over traditional manufacturing methods. These benefits include cost and lead time reduction, minimal waste generation, and the production of near-net-shape parts [1,2]. Among the different MAM technologies, many of the most widespread (such as laser powder bed fusion, direct energy deposition, or cold spray) use metal powders as starting material; as a result, to optimize component production, powder properties such as particle shape, size, and microstructure are crucial to produce components with high density and mechanical properties [3,4].

Metal powders for MAM can be produced through various processes including solid-state reduction, electrolysis, and chemical methods [5]. Nevertheless, atomization is the prevailing technique used to transform molten metal, in form of bulk fluid, into a spray system by means of an inert gas or a water jet [5]. The process involves rapid solidification of the liquid droplets after being atomized through the nozzle [5]. Among various atomization techniques, inert gas atomization, using nitrogen or argon, stands out with numerous advantages, including the production of highly spherical and fine particles with high

atomization yield [5,6]. Achieving sphericity, as well as minimizing the presence of satellites and impurities is, in fact, crucial to obtain powders with high flowability, necessary for the optimization of those MAM processes that use powders as feedstock materials. The exceptionally high cooling rates ($\approx 10^{-4}$ K·s^{-1} [7]) occurring during gas atomization result in spherical particles with microstructures that are fundamentally distinct from those found in wrought or casting materials of the same alloy composition [8]. However, the microstructure of the powders obtained with this process may be not homogenous, and different powder microstructures can be present even within the same batch, as the cooling rates for individual powder particles vary according to their size [9].

Despite recent advancements, one of the main limitations of MAM technology is the limited availability of processable materials. Typically, stainless steel, Ti6Al4V, Inconel 625, Inconel 718, and AlSi10Mg [3,10–15] are the most extensively studied materials. Among these alloys, aluminum alloys stand out as some of the most interesting materials due to their low specific weight, excellent strength-to-weight ratio, intrinsic corrosion resistance, good thermal and electrical conductivity, and optimal formability and machinability [16]. However, the Al alloys available on the market today are primarily designed for conventional manufacturing methods and not specifically tailored for additive manufacturing processes. They generally reach yield strengths in the 150–300 MPa range, failing to meet the growing need for higher strength levels [17], as they are characterized by moderate strength and hardness and low toughness in the as-processed state.

To enhance the mechanical properties of Al and Al alloys, recent studies have investigated the effect of the incorporation of pure Cu, a well-established strengthening agent [18–21] through the precipitation of the θ′ phase (Al_2Cu) [22,23]. In particular, numerous investigations have been presented in the literature on the microstructure of gas-atomized Al-Cu binary alloys [7,8,24–27]. Liu et al. conducted a study on Al-Cu powders with copper content ranging from 2 to 5 wt% and particle sizes of 10–40 µm. Their findings revealed a cellular microstructure attributed to the exceptionally high cooling rate of the process, with the θ phase located along the cell boundaries [8]. Furthermore, the addition of copper resulted in a more continuous θ phase network, a slight reduction in cellular spacing, and the increased hardness of the powders as the copper content increased. Bedel et al. studied aluminum with 4.5 wt% Cu with particle sizes ranging from 250 to 300 µm. They documented the presence of a dendritic microstructure characterized by four distinct morphologies, namely, highly branched, highly branched with visible primary arms, dendritic, and "finger bundle." The formation of these morphologies was found to be dependent on the cooling rate during the atomization process [25,26] and thus on the particle size.

To enhance the creep resistance and tensile strength at room temperature, several studies also reported the effect of copper in the Al-Si-Cu-Mg quaternary system [28,29]. The Al-Si-Mg-Cu alloys are, in fact, characterized by the Q-phase precipitation (Al4Cu2Mg8Si7) that, in the casting process, can be obtained after heat treatments within the temperature range of 200 to 300 °C. The precipitated Q phase is characterized by lath or needle-like structures spanning hundreds of nanometers, and it plays a vital role in improving mechanical properties by facilitating Orowan strengthening.

To the authors' knowledge, there is only one work in the literature on gas-atomized powders belonging to the Al-Si-Cu-Mg quaternary system [30]. Martin et al. produced a AlSi10Mg4Cu alloy to investigate the influence of the addition of Cu on the microstructure and microhardness of an AlSi10Mg alloy processed by laser powder bed fusion (L-PBF) [30]. Their powders, with particle sizes ranging from 20 to 63 µm, showed a dendritic microstructure composed by an α-aluminum matrix and an interdendritic channel populated by the Si-eutectic phase and the θ phase.

The Al-Si-Cu-Mg system is promising for MAM technologies as also underlined by Bosio et al. who, using L-PBF, successfully obtained AlSi10Mg samples with an addition of 4 wt% copper [18]. In their work, the authors processed the material using a mechanically mixed powder obtained by ex situ milling with a drum mixer. Nanoindentation tests

showed an increase in hardness for the Cu-added samples with respect to that of the base AlSi10Mg alloy, even if the samples exhibited compositional variations and a non-homogeneous distribution of copper, primarily due to differences in the physical properties, such as melting temperature, of the used powders [18,31].

Based on these interesting results, the aim of this work is to evaluate the possibility of obtaining powders by gas atomization, specifically tailored for MAM, with a copper content well above the equilibrium solubility limit in the Al-Cu binary system (5.65 wt% at the eutectic temperature) to enhance the mechanical properties. Close-coupled gas atomization (CCGA) was employed to produce AlSi10Mg powders with an increasing amount of copper (4, 8, and 20 wt%), and a comprehensive characterization of powders was performed to investigate the evolution of phase content, microstructure, and mechanical properties as a function of copper content increase. Initially, a simulation using Thermo-Calc software was conducted to predict the formation of phases and their respective quantities in the system. These outcomes were then compared with experimental results including X-ray diffraction (XRD), scanning electron microscopy (SEM), and transmission electron microscopy (TEM). Finally, hardness testing was carried out to further examine the powders' mechanical properties.

2. Materials and Methods

Powders with a composition AlSi10Mg + X Cu with copper contents of 0, 4, 8, and 20 wt% were produced using gas atomization. The process was carried out using a HERMIGA 100/10 VI gas atomizer provided by Phoenix Scientific Industries (Phoenix Scientific Industries Ltd., Hailsham, East Sussex, UK), utilizing the experimental setup described in Marinucci et al. [32]. Starting from the AlSi10Mg system and progressively adding pure copper element to obtain the desired compositions, the gas atomization process was carried out using an alumina crucible with a capacity of 10 kg of steel, or equivalent volumes, and the molten metal was forced to pass through a nozzle with a diameter of 2.5 mm. Before the vacuum induction melting, a backfill process was performed to prevent elements with a low boiling point (or high vapor pressure), i.e., Mg, from evaporating. The melting temperature was set at 800 °C for the AlSi10Mg alloy and 1150 °C for alloys containing copper. During atomization, a gas pressure of 40 bar was applied, while a pressure of 0.25 bar was maintained in the melting chamber. To avoid problems related to oxidation, the entire gas atomization process was conducted in an atmosphere of high-purity argon gas. After the gas atomization process, ICP analyses were performed using an ICP/MS ICAPQ (Thermo Fisher Scientific Inc., Waltham, MA, USA), and the resulting chemical compositions of the powders (Table 1) underlined that the chemical composition of the obtained powders is comparable to the nominal one.

Table 1. Powders' chemical compositions after the gas atomization process.

	Al (%)	Si (%)	Cu (%)	Mg (%)
AlSi10Mg	Bal.	11.94 ± 1.96	/	0.54 ± 0.33
+4% Cu	Bal.	10.41 ± 4.18	4.58 ± 1.23	0.43 ± 0.22
+8% Cu	Bal.	9.95 ± 5.58	8.52 ± 1.98	0.41 ± 0.24
+20% Cu	Bal.	10.01 ± 5.51	20.90 ± 3.82	0.66 ± 0.55

The powders were carefully sieved in the 20–50 µm range, which is considered suitable for many MAM technology applications. The powders exhibited a spherical shape as confirmed by roundness values of 0.83, 0.88, 0.81, and 0.82 obtained for the AlSi10Mg, +4% Cu, +8% Cu, and 20% Cu alloys, respectively. Further analyses of the characteristics of the powders in terms of morphology and flowability are reported in a previous work [33].

To gain insights into the phase composition and their respective quantities, simulations were first conducted using Thermo-Calc (Thermo-Calc Software version 2022b, TCAL7, and MOBAL6 databases). These simulations encompassed two conditions: equilibrium, employing the "lever rule", and non-equilibrium, using the Gulliver–Scheil (GS) model to

account for the high cooling rate and rapid solidification characteristics of the atomization process, as previously utilized by Bogno et al. and Prasad et al. [24,34]. In particular, the 'Classic Scheil Model' was employed, which assumes that the diffusion of all elements in the liquid phase is infinitely fast, there is no diffusion of elements in the solid phases, and the liquid/solid interface is in thermodynamic equilibrium.

To compare the data predicted by Thermo-Calc with experimental data, X-ray diffraction (XRD) measurements were conducted using an X'Pert Philips diffractometer (PANalytical, Almelo, The Netherlands). The measurements were performed on the as-atomized powders (non-equilibrium condition) as well as on heat-treated powders subjected to a temperature of 300 °C for 100 h (equilibrium condition). The XRD analyses were carried out in a Bragg–Brentano configuration, covering a 2θ range from 15 to 140° 2θ. The measurements employed a step size of 0.005° with a duration of 0.5 s per step. To ensure accuracy, high-purity silicon powder was used as a standard reference material. The Rietveld refinement software Profex v5.1.0 (Nicola Döbelin, Solothurn, Switzerland) as used to determine the phase fraction and lattice parameters of the powders [35]. Refinement was carried out until a Rwp of less than 10% and a GoF value in the range of 1–2 were reached.

To analyze the microstructure, the powder particles were embedded in Polyfast resin and prepared for cross-sectional examination. The samples were mechanically ground, polished down to 1 µm, and further refined to 0.02 µm using a vibratory polisher with colloidal alumina polishing suspension for 2 h. For scanning electron microscopy (SEM) analysis, the mounted powders were etched with Kroll's etchant for 10 s. Conversely, for electron backscattered diffraction (EBSD) analysis, the samples were left as polished.

The SEM analysis was conducted using the Apreo S FE-SEM (Thermo Fisher Scientific Inc., Waltham, MA, USA) at an accelerating voltage of 20 keV. To determine the secondary dendrite arm spacing (SDAS) for each composition, ten measurements were taken on ten particles, with a minimum of 100 measurements obtained for each composition [7].

The EBSD measurements were performed using a step size of 150 nm at an accelerating voltage of 20 keV using the JEOL 7000 FE-SEM (JEOL Ltd., Tokyo, Japan) equipped with the Oxford AZtec EBSD system. The EBSD data, used for the grain-size analysis, were processed using AZtech Crystal software (https://www.ebsd.com/ois-ebsd-system/azteccrystal-processing-software), which included noise reduction and extrapolation of zero solutions using five neighbors. The grain-size data were then used to fit an empirical cumulative distribution function for comparison between the grain-size distributions of the different powder compositions. The critical misorientation for grain detection was set to 10°.

The compositional analyses of the powders were carried out using the SEM Phenom Pro XL (Thermo Fisher, Waltham, MA, USA) and the FEI Tecnai F-20 Scanning/Transmission Electron Microscope ((S)TEM) operating at 200 keV (Thermo Fisher, Waltham, MA, USA) equipped with a EDAX TEAM Octane T Optima detector. The line scan was collected using a step size of 7 nm and a dwell time of 100 ms, and was processed with TEAM software (https://www.edax.com/). The same TEM instrument was used for TEM imaging and electron diffraction. The TEM samples were prepared starting from samples analyzed by SEM using the FEI Quanta 3D Dual Beam (Thermo Fisher, Waltham, MA, USA), a focused ion beam (FIB) instrument. Sections with dimensions of approximately 15 µm in length, 1 µm in width, and 5 µm in depth were milled using a gallium ion beam at 30 keV. Subsequently, the lift-out specimens were thinned to electron transparency (<100 nm) and polished at 5 keV using the Tescan Lyra FIB-FESEM (Tescan, Brno, Czech Republic).

Finally, to assess the mechanical properties, the hardness of the as-atomized powders was measured on the powder particle cross-section previously mounted and polished for SEM imaging using the Matsuzawa MMT-X7B hardness tester (Clemex Technologies Inc., Brossard, QC, Canada). Ten measurements were performed for each sample with a load of 3 g applied for 12 s.

3. Results and Discussion

3.1. AlSi10Mg + X wt% Cu Alloy Simulation

To investigate the effect of copper addition on the AlSi10Mg system, a preliminary simulation was conducted using the Thermo-Calc software to evaluate the phases formed during the solidification process and their relative quantities within the system. The evaluation was performed by considering two different conditions, equilibrium and non-equilibrium, as expected due to the gas atomization process. The non-equilibrium simulation in Thermo-Calc uses a Gulliver–Scheil approach to account for solute redistribution in the liquid. Figure 1 illustrates the obtained results for the alloys under investigation.

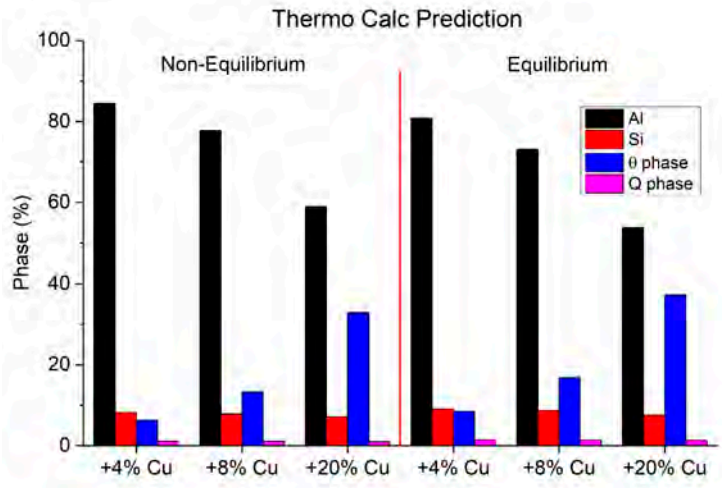

Figure 1. Phase prediction and quantification for the new AlSi10Mg + X wt% Cu alloys using Thermo-Calc software.

All considered compositions, in both equilibrium and non-equilibrium conditions, consisted of four distinct phases: aluminum, silicon, θ phase (Al_2Cu), and Q phase (Al4Cu2Mg8Si7). In the non-equilibrium condition, by increasing the copper content, the α-aluminum phase amount decreased, while the θ phase content increased. Conversely, the Si and Q phase contents did not significantly change from values of approximately 8% and 1%, respectively. The low Q-phase content was compatible with the Mg content, which remained constant in the four powders. Moreover, it is evident from these data that the θ and Q phases, which are the primary strengthening phases in Al-Cu-Mg-Si alloys, could already be formed during the atomization process without the necessity of any post heat treatment.

Considering the equilibrium condition, the behavior of the Al and θ phases as the copper content increased, was quite similar to that of non-equilibrium, even though the relative amount of these phases was different. In fact, it can be observed that under equilibrium conditions, the content of θ phase was higher than under non-equilibrium conditions. Unexpectedly, however, the content of the Q phase, as well as that of Si, did not significantly vary if the two cooling conditions were compared.

3.2. Phase Analysis

X-ray diffraction (XRD) analyses were conducted to experimentally determine the phase composition of the gas-atomized systems and validate the predictions obtained by Thermo-Calc. The normalized XRD patterns (with respect to the highest intensity peak of Al (111)) of the AlSi10Mg + X wt% Cu powders are presented in Figure 2, representing both the as-atomized condition and the annealed condition (300 °C for 100 h, chosen according to Farkoosh et al. [29]) to simulate non-equilibrium (Figure 2a) and equilibrium states (Figure 2b). Unlike the AlSi10Mg alloy, the XRD patterns of the atomized powders containing copper exhibited the presence of three phases in both as-atomized and annealed conditions: an α-Al phase with a face-centered cubic (FCC) structure, a Si-eutectic phase

with an diamond-cubic structure, and an intermetallic θ (Al_2Cu) phase with a body-centered tetragonal (BCT) structure, confirming that this phase was primarily formed during the solidification process even under very fast cooling conditions. The patterns did not show, under either condition, the presence of Q phase which, if present, may be in a quantity below the instrument detection limit.

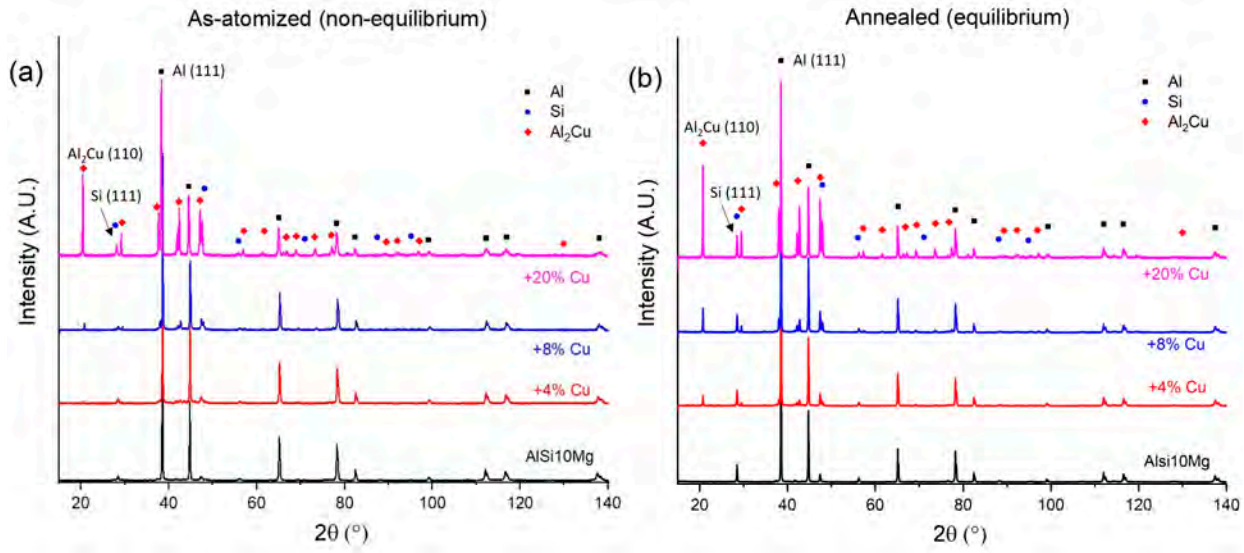

Figure 2. XRD patterns of AlSi10Mg + X wt% Cu powders in (**a**) as-atomized and (**b**) annealed conditions.

The patterns consistently showed dominant peaks corresponding to the α-Al phase, indicating its presence as the matrix phase, while the intensity of peaks associated with the Si-eutectic phase (see, for example, the peak Si(111) highlighted in Figure 2) remained relatively stable as the copper content increased in both conditions but was lower in the as-atomized condition compared to the annealed condition. The intensity of the θ phase peaks (see, for example, the peak Al_2Cu(110) highlighted in Figure 2) increased with copper content, in agreement with the Thermo-Calc simulation, and, as observed for the Si-eutectic phase, was lower in the as-atomized condition compared to the annealed condition. This behavior can be attributed to the accelerated solidification rate involved in gas atomization, which inhibits the precipitation process and increases the solubility of copper in non-equilibrium conditions.

In Figure 3, a specific detail of the XRD patterns depicting the (420) Al peak of the AlSi10Mg + X wt% Cu powders is reported. It can be noted that, in the as-atomized powders, the peak shifted towards higher 2θ angle values, with respect to the AlSi10Mg alloy, as the copper content increased. This lattice distortion in the α-Al solid solution phase can be attributed to the contraction of the crystalline lattice with the copper content increase due to the lower atomic size of copper (127.8 pm) with respect to aluminum (143.1 pm). By comparison, after a long anneal (100 h) at 300 °C, the (420) reflections of the α-Al solid solution phase were all well-aligned, showing that the four annealed powders were at equilibrium.

To better evaluate this behavior, the Rietveld refinement method was utilized to determine the lattice parameters of each phase in both as-atomized and annealed powders (Table 2).

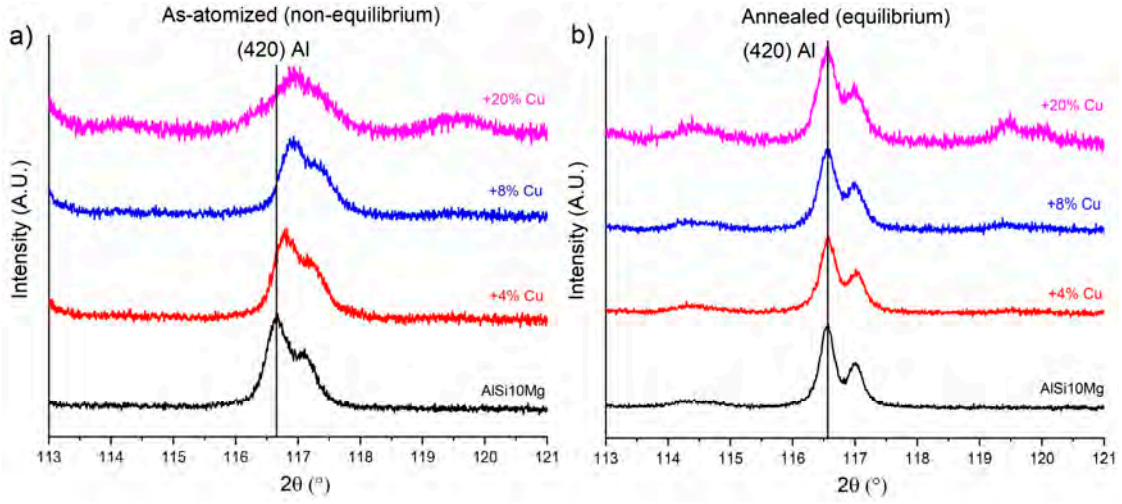

Figure 3. Detail of the XRD pattern showing the (420) Al peak of (**a**) the as-atomized and (**b**) annealed AlSi10Mg + X wt% Cu powders.

Table 2. Refined lattice parameters for as-atomized and annealed powders.

Condition	Cu Content (wt%)	Al, a(Å)	Si, a(Å)	ϑ, a(Å)	ϑ, c(Å)
As-atomized	0	4.048(1)	5.433(3)	/	/
	4	4.044(1)	5.429(2)	6.067(2)	4.882(1)
	8	4.042(1)	5.432(1)	6.065(1)	4.877(1)
	20	4.042(1)	5.438(2)	6.063(1)	4.878(1)
Annealed	0	4.050(1)	5.426(1)	/	/
	4	4.050(1)	5.426(2)	6.062(1)	4.871(1)
	8	4.050(1)	5.426(1)	6.064(1)	4.867(1)
	20	4.050(1)	5.426(1)	6.063(1)	4.870(2)

The standard lattice parameter values for Al, Si, and θ are as follows: Al (a = 4.049 Å, from ICDD 000040787), Si (a = 5.431 Å, from ICDD 000271402), and θ (a = 6.067 Å, c = 4.877 Å, from ICDD 010891980). These values closely matched the refined lattice parameters obtained for all annealed powders, indicating the complete precipitation of the phases due to the heat treatment. On the contrary, the as-atomized powders exhibited a distinct behavior. The refined lattice parameter of the α-Al phase experienced, as expected from Figure 3, a gradual reduction with increasing copper content, as also reported by Liu et al. and Zhang et al. [8,36]. As previously stated, rapid cooling confines the Cu atoms within the Al matrix, resulting in lattice distortion due to the disparity in atomic sizes [8,36]. Moreover, the rapid solidification process could induce the formation of vacancies and dislocations within the powders, thereby exacerbating lattice distortion [8,36]. Beyond 8 wt%, no additional variations in the lattice parameter were discernible. This phenomenon can be explained by considering the maximum solubility limit of 5.65 wt% of Cu in the Al matrix, as indicated by the Al-Cu phase diagram. Finally, both the a-axis and c-axis lattice parameters for the θ phase were in good agreement, independently of the copper content and cooling conditions, with the standard values.

The Rietveld refinement method, employed for determining the lattice parameters of each phase fraction, was also utilized to assess the fraction of each phase in the different powders (Figure 4).

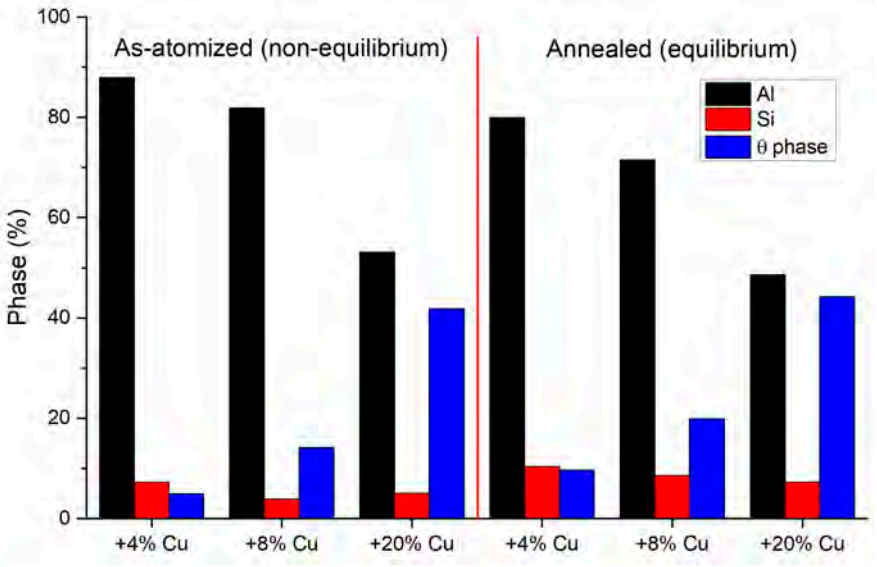

Figure 4. Refined phase fraction for the as-atomized and annealed powders.

The refinement analysis confirmed the behaviors revealed by the XRD analysis, showing that the Si phase is almost constant with increasing copper content. Moreover, as already suggested by the peak intensity analysis, it is less abundant in the as-atomized state when contrasted with the annealed condition. Finally, this refinement revealed that as the copper content increased, the fraction of the θ phase linearly increased in both the annealed and as-atomized conditions. In particular, the θ phase fraction was slightly higher in the annealed condition compared to the as-atomized condition, confirming that the θ phase almost completely precipitates during the atomization process, especially with the higher Cu content. It is evident, comparing the data obtained using Thermo-Calc and Rietveld (Figure 5), that the simulations underestimate the amount of θ-phase present in the alloy especially when the copper content is 20 wt% (about 9% and 7% under non-equilibrium and equilibrium conditions, respectively).

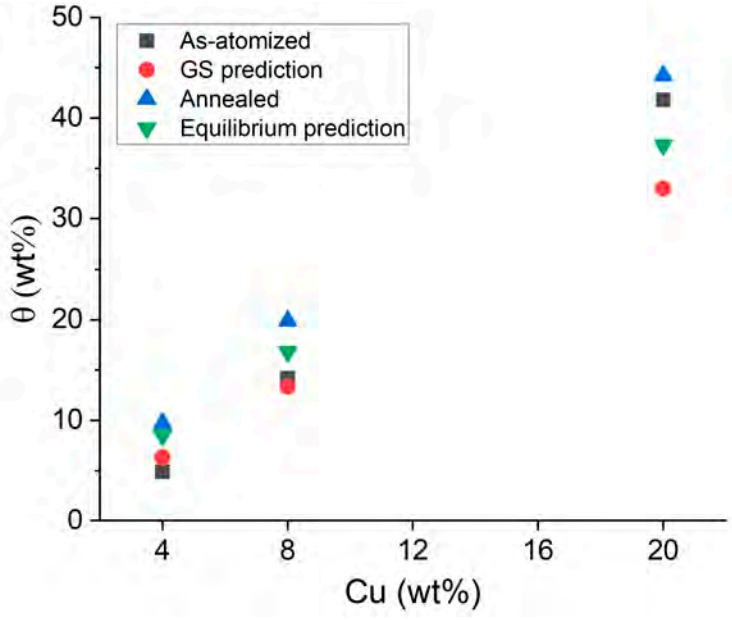

Figure 5. Percentage by weight of the θ phase with varying copper content, as determined through Rietveld analysis, the lever rule, and the Gulliver–Scheil (GS) model.

This result is consistent with the findings reported by Liu et al. in the binary system, where the copper content was below the solubility limit, specifically, up to 5.5 wt% Cu [8]. However, when dealing with alloys containing a copper content exceeding this limit, the Gulliver–Scheil (GS) model can only be used as a starting point for predicting the phases present in the powders after gas atomization. In conclusion, the agreement between the GS and Rietveld model results for as-atomized powders is still good up to 8 wt% Cu; however, GS does not hold for 20 wt% Cu.

3.3. Microstructure Analysis

The microstructure of the gas-atomized Al-Si-Cu-Mg powders is illustrated in Figure 6 through secondary electron (SE) and backscattered electron (BSE) SEM images. All powders presented a dendritic solidification microstructure composed of an α-Al matrix phase and an interdendritic network. The site of solid nucleation was unclear from the cross-sections of the particles. Figure 6a shows the AlSi10Mg powder, which exhibited a larger secondary dendrite arm spacing (SDAS) compared to the other alloys, with an average size of 2.19 ± 0.56 µm. Figure 6e reveals two distinct phases: a dark grey phase representing the α-Al matrix phase, and a light grey phase corresponding to the Si-eutectic phase. A similar microstructure was observed by Albu et al. [37]. In their study, they also identified the matrix as the α-Al phase, while the interdendritic network consisted of the eutectic silicon phase composed of crystalline nanoparticles, along with an amorphous or disordered crystalline phase [37]. The SE images of the 4, 8, and 20 wt% Cu alloys (Figure 6b–d) demonstrate that an increase in copper content results in a higher fraction of the interdendritic phase and a reduction in the size of the SDAS: 1.33 ± 0.36 µm, 0.98 ± 0.23 µm, and 0.69 ± 0.15 µm, respectively. This phenomenon had previously been documented in the research conducted by Shabestari and Moemeni, who investigated an Al-Si-Mg alloy with varying copper content in the range of 0.2–2.5 wt% [38]. Their study revealed that altering the mold material, and thereby modifying the cooling rate, resulted in distinct SDAS outcomes. In every mold, it was evident that as the copper content increased, the SDAS decreased. The BSE images (Figure 6f–h) reveal the presence of a new brighter phase, which corresponds to the θ phase as suggested by the XRD results. This phase, uniformly distributed within the powder particles, increases with higher copper content, and is located in the interdendritic channels alongside the Si-eutectic phase. This occurrence can be attributed to the rapid solidification process, whereby the solute copper and silicon are pushed out towards the liquid at the boundaries of the dendrites. As a result, during the rapid solidification, their concentration in the interdendritic liquid rises, eventually reaching the eutectic composition, leading to the formation of the Si-eutectic and, subsequently, the θ phases.

To confirm this microstructure analysis, an SEM EDS analysis was performed. Figure 7 displays the EDS SEM map of the +8%Cu powder, which is representative of all powders. The analysis confirmed that aluminum (red color) was the predominant element present in the powder and was present in every phase. Silicon (green color) was discovered within the interdendritic eutectic network, whereas copper (blue color) occupied the interdendritic channels as part of a distinct phase in contrast to silicon. These findings were in full agreement with the observations made using BSE imaging, and confirmed the θ phase as the brighter phase. We note that, at the 0.5 wt% level of Mg in this alloy, no measurable variation in the EDS signal for Mg was observed across the sample.

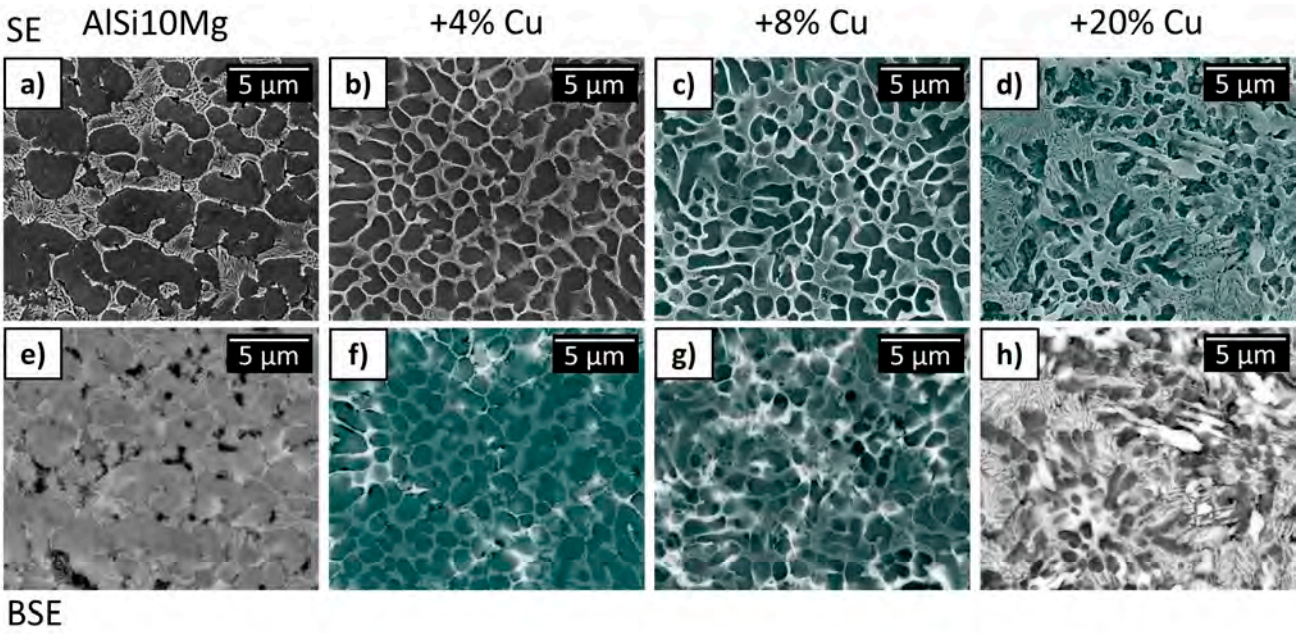

Figure 6. Secondary electron (SE) (**a**–**d**) and backscattered electron (BSE) (**e**–**h**) images of the cross-section of etched as-atomized AlSi10Mg + X wt% Cu powders. The black spots are an artifact generated during the etching of the samples with Kroll's reagent.

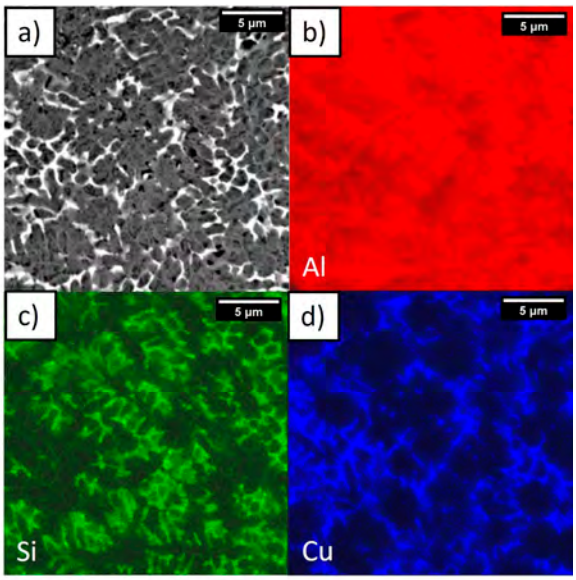

Figure 7. EDS SEM maps of the +8% Cu alloy: (**a**) BSE image, (**b**) Al map, (**c**) Si map, and (**d**) Cu map.

As previously mentioned, during the rapid cooling process, copper and silicon are pushed towards the liquid at the boundaries of the dendrites due to the high cooling rate. This phenomenon, as reported by Liu et al. [8], can result in a variation in the Cu content within the same cell. TEM EDS line scans were conducted to assess the Cu content distribution within the aluminum matrix. Figure 8 presents the results of the TEM EDS line scan analysis performed on the +20%Cu sample, which had the highest Cu content and can be considered as representative of the other samples. The X-ray line scan from the TEM data indicates that there was no variation in the copper content within the same dendrite arm, and the only variation in Cu content was detected in the presence of the θ phase, at the dendrite boundaries.

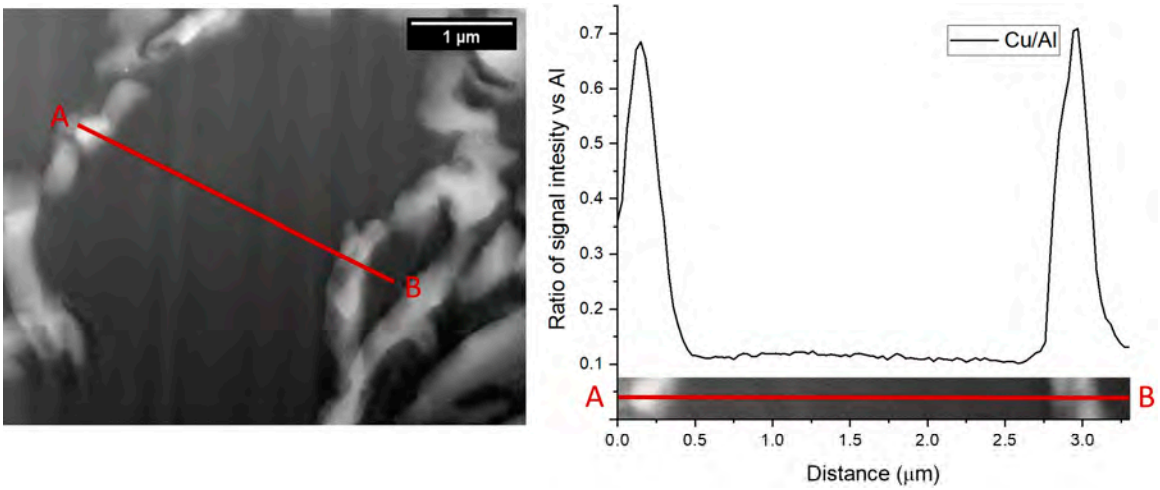

Figure 8. STEM HAADF image and corresponding TEM EDS line scan of the +20%Cu alloy.

To assess the presence of the Q phase, additional TEM EDS analyses were performed on the powder samples. Figure 9 shows the STEM picture and the EDS TEM map of the +8%Cu powder, serving as a representative sample for all copper-containing powders. Notably, the STEM image (Figure 9a) depicts various dendritic arms and their corresponding interdendritic channels. It is possible to observe, as previously noted in Figure 5, the presence of three distinct phases: an α-Al matrix (grey phase), a eutectic silicon (dark grey phase), and a θ phase (brighter phase) in interdendritic channels. Furthermore, the TEM EDS maps of Al, Si, and Cu (Figure 9b,c,e) reveal the same elemental distribution observed in the SEM EDS analyses, but the Mg map (Figure 9e) reveals some precipitates containing Mg. These precipitates, of a few hundred nanometers in size, consist of Mg, Al, Si, and Cu, and they were situated in the interdendritic channels. This composition could be attributed to the Q phase, thereby suggesting its presence within the powders. These findings contrast with the observations made in the AlSiCu4Mg powder's TEM analyses by Martin et al. [26], where no agglomerates of Mg were detected, but agree with the Thermo-Calc simulation. So, the prediction of the Q phase in the simulation using Thermo-Calc was partially supported by these findings, even if we cannot definitively confirm its presence within the powders.

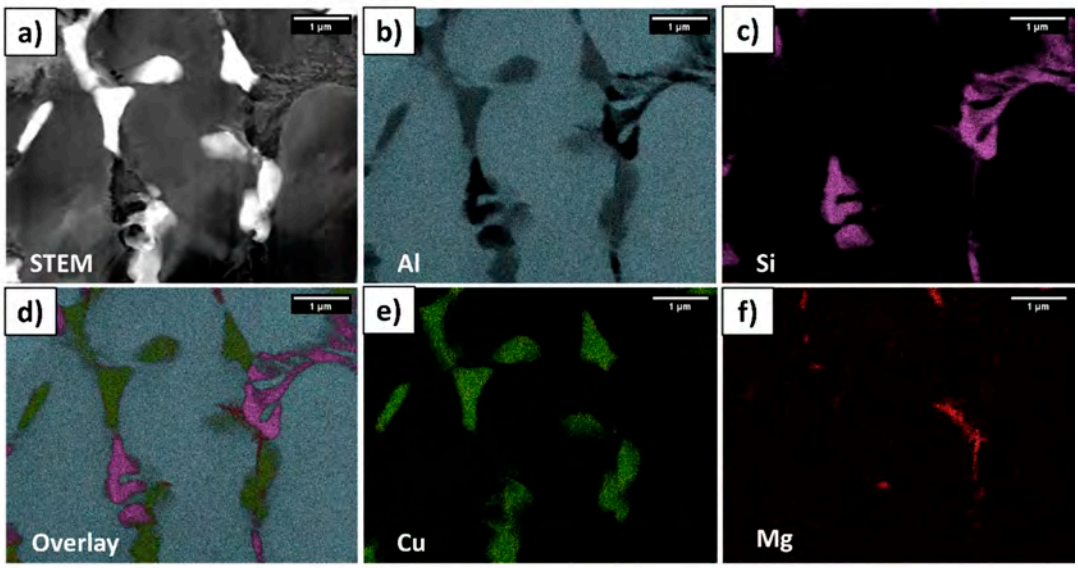

Figure 9. EDS TEM Maps of the +8%Cu alloy: (**a**) STEM image, (**b**) Al map, (**c**) Si map, (**d**) overlay map, (**e**) Cu map, and (**f**) Mg map.

3.4. Grain Structure Analysis

The EBSD data regarding the band contrast, phase map, and aluminum grain map are reported in Figure 10. The band contrast images (Figure 10a,d,g,f) showed that many secondary dendrite arms (SDA) can be contained in a single grain. The phase map (Figure 10b,e,h,k) illustrates the distribution of the θ phase (blue areas) within the interdendritic channels that increases with the copper content, as already seen in the BSE images (Figure 6f–h), and appears to concentrate at grain boundaries rather than being uniformly distributed. In Figure 10b, it is noticeable that there is a higher presence of the Si (21.8%) phase (green areas) compared to the other maps (Figure 10e,h,k), although the quantity of silicon should be very similar among the four analyzed powders. However, in the EBSD analysis, it is difficult to clearly distinguish the Al and Si phases because they have very similar space groups (#225 and #227, respectively), which can be challenging to consistently differentiate using standard Hough transform-based indexing with EBSD data [39]. Therefore, during the analysis, the Si microstructure merges with the Al one. For this reason, the AlSi10Mg powder map was not reliable, and only the powders containing copper were considered for the grain analysis.

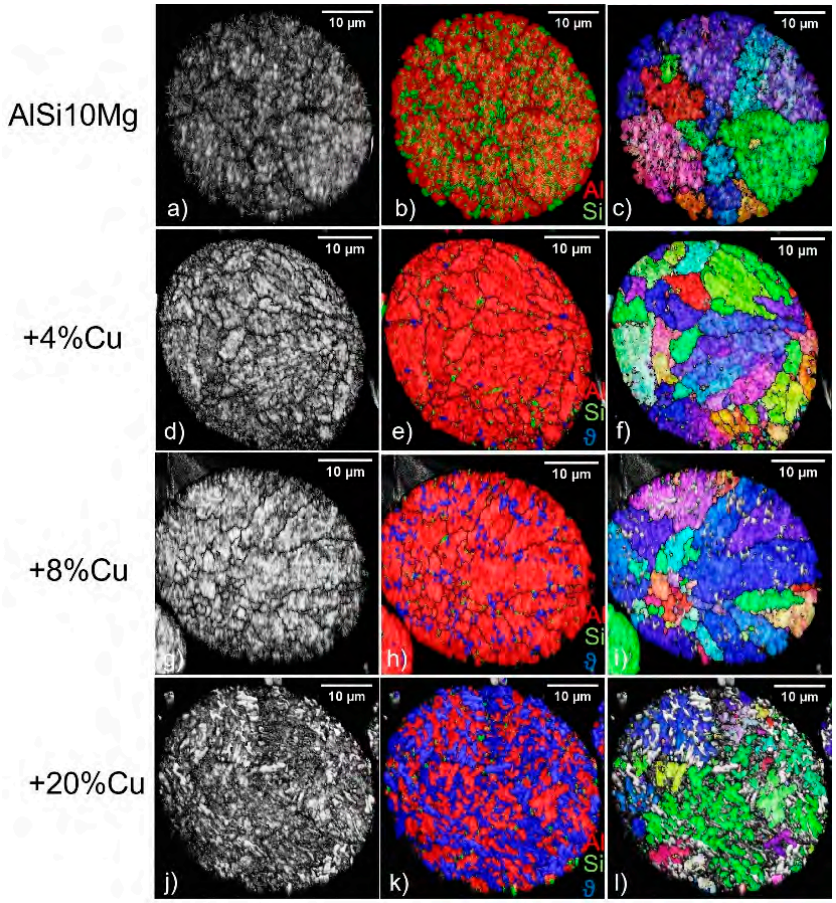

Figure 10. EBSD measurements of the AlSi10Mg (**a**–**c**), +4%Cu (**d**–**f**), +8%Cu (**g**–**i**) and +20%Cu (**j**–**l**) powders: (**a**,**d**,**f**,**g**) band contrast, (**b**,**e**,**h**,**k**) phase map with Al (red) Si (green), and θ phase (blue), and (**c**,**f**,**i**,**l**) aluminum grain map.

In the aluminum grain maps (Figure 10f,i,l), it can be observed that the grain size decreased as the copper content increased. This trend is highlighted in Figure 11, which shows the aluminum grain size represented as a cumulative distribution function (CDF). The alloy with +4% Cu exhibited larger aluminum grains compared to the +8% and +20% alloys, and the grain size decreased as the copper content increased, following a similar trend as the SDAS.

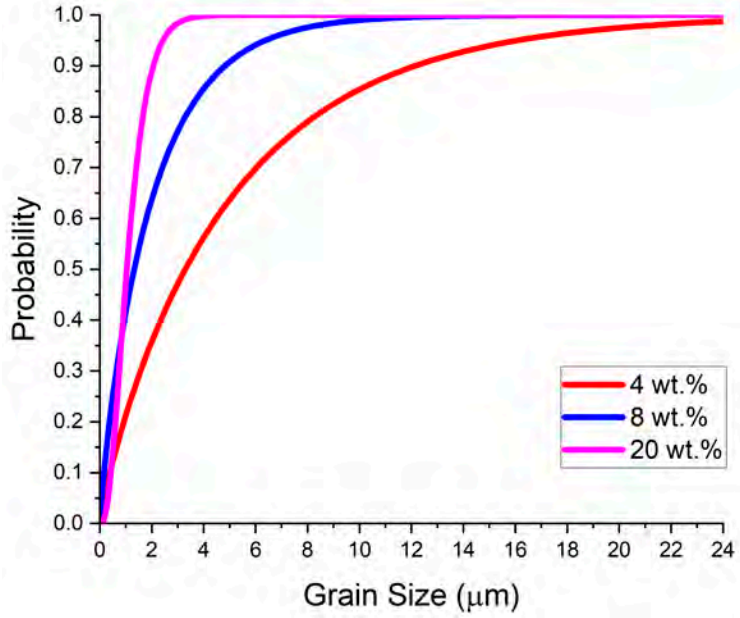

Figure 11. Aluminum grain size against cumulative density function (CDF).

3.5. Hardness of As-Atomized Powders

Hardness tests were performed in order to compare the mechanical properties of the four powders under investigation. As expected from the literature [40], the data clearly demonstrate that the addition of copper significantly influences the properties of the AlSi10Mg alloy, increasing its hardness; the trend of experimental data shown in Figure 12 evidences a linear increase in hardness as the copper content increases. Notably, the hardness value of 185 ± 13 HV of the +20%Cu alloy was found to be twice that of the AlSi10Mg alloy (88 ± 5 HV). The increase in hardness and, consequently, the expected enhancement of mechanical properties can be attributed to multiple factors. Firstly, it can be linked to the reduction in the size of dendrite arms, a phenomenon also reported by Ghassemali et al. for an Al-Si cast alloy. However, the primary contributing factor likely arises from the linear increase in the θ phase content with increasing copper levels (Figure 5), which exhibits a parallel behavior with hardness [38].

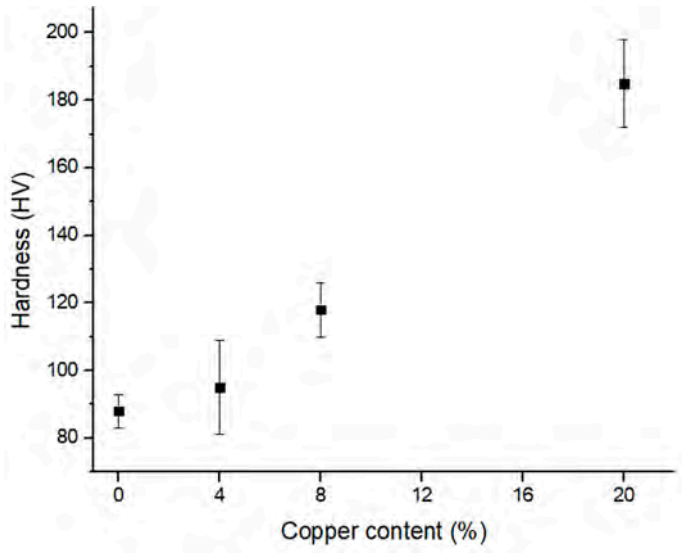

Figure 12. Hardness measured against copper content.

These hardness results can be compared with the findings obtained by Martucci et al. [41]. In their work, bulk samples were produced starting from the same powders using the L-PBF process, resulting in hardness values that are approximately 50–70% higher but with the same trend as a function of copper. Apart from the completely similar behavior as a function of copper content, the difference in the obtained values could be attributed to various factors, but, in principle, to the methodology of microhardness measurements, which were conducted here on embedded powders, possibly leading to variations in values due to the used resin. Nevertheless, it can be said that the analysis performed on powders makes it possible to assess, with a certain degree of approximation, the hardness values that can be obtained in printed parts.

4. Conclusions

The comprehensive examination of powders from a newly atomized alloy holds significant importance due to its potential in providing predictive insights into the microstructural attributes and mechanical properties of the bulk samples manufactured using MAM technologies.

In this study, the powders of the AlSi10Mg alloy and three alloys obtained by adding 4, 8, and 20 wt% of copper were successfully produced through inert gas atomization. These powders were analyzed to examine the evolution of the microstructure and hardness with varying copper content. The characterization of the obtained powders revealed the following observations:

- The hardness value increased linearly with increasing copper content, and the hardness value of 185 $\pm$ 13 HV of the +20%Cu alloy was found to be twice that of the AlSi10Mg alloy (88 $\pm$ 5 HV), reaching the goal of this study.
- The increase in hardness can be attributed to the reduction in secondary dendrite arm cell size, which was initially very small (3 μm) and decreased as the copper content increased (0.5 μm for the +20%Cu alloy). A similar trend was observed when analyzing the grain or crystallite size.
- The increase in hardness can also be attributed to the increase in the θ phase content, which increased linearly as the hardness increased with the copper content.
- The GS model can be used for predicting the phase content of these alloys for low Cu content (up to 8 wt%), but it is not suitable beyond this limit because it underestimates the phase content.
- The presence of a nanometric Mg-rich phase (probably Q phase) and θ phases in the as-atomized powders enables the utilization of these powders in additive manufacturing processes that do not require powder fusion, such as the cold spray process, even without additional heat treatments.

In conclusion, these promising results create opportunities for future research into the processability and optimization of process parameters for these alloys, using additive manufacturing techniques such as cold spray, L-PBF, and EB-PBF.

Author Contributions: Conceptualization, L.N.B., F.B. and M.W.; methodology, L.I.P.-A. and M.W.; software, M.V., M.J.P. and C.J.W.; validation, E.P., L.I.P.-A. and L.N.B.; formal analysis, M.V., M.J.P. and C.J.W.; investigation, M.V., E.P. and F.B.; resources, M.V., M.J.P. and C.J.W.; data curation, M.V., M.J.P. and C.J.W.; writing—original draft preparation, M.V.; writing—review and editing, E.P., F.B. and L.N.B.; visualization, E.P. and L.I.P.-A.; supervision, F.B., M.W. and L.N.B.; project administration, P.F., F.B. and L.N.B.; funding acquisition, P.F., F.B. and L.N.B. All authors have read and agreed to the published version of the manuscript.

Funding: This research received no external funding.

Data Availability Statement: Not applicable.

Acknowledgments: A special acknowledgement goes to Federico Gobber, Enrico Virgillito, and Fabrizio Marinucci, who contributed to the powder gas atomization, and to Rheka Y. Rao for the TEM sample preparation.

Conflicts of Interest: The authors declare no conflict of interest.

References

1. Attaran, M. The Rise of 3-D Printing: The Advantages of Additive Manufacturing over Traditional Manufacturing. *Bus. Horiz.* **2017**, *60*, 677–688. [CrossRef]
2. Padovano, E.; Badini, C.; Pantarelli, A.; Gili, F.; D'Aiuto, F. A Comparative Study of the Effects of Thermal Treatments on AlSi10Mg Produced by Laser Powder Bed Fusion. *J. Alloys Compd.* **2020**, *831*, 154822. [CrossRef]
3. Frazier, W.E. Metal Additive Manufacturing: A Review. *J. Mater. Eng. Perform.* **2014**, *23*, 1917–1928. [CrossRef]
4. Chowdhury, S.; Yadaiah, N.; Prakash, C.; Ramakrishna, S.; Dixit, S.; Gupta, L.R.; Buddhi, D. Laser Powder Bed Fusion: A State-of-the-Art Review of the Technology, Materials, Properties & Defects, and Numerical Modelling. *J. Mater. Res. Technol.* **2022**, *20*, 2109–2172. [CrossRef]
5. Wallner, S. Powder Production Technologies. *Berg Huettenmaenn. Monatsh.* **2019**, *164*, 108–111. [CrossRef]
6. Zheng, B.; Lin, Y.; Zhou, Y.; Lavernia, E.J. Gas Atomization of Amorphous Aluminum Powder: Part II. Experimental Investigation. *Met. Mater. Trans B* **2009**, *40*, 995–1004. [CrossRef]
7. Mullis, A.M.; Farrell, L.; Cochrane, R.F.; Adkins, N.J. Estimation of Cooling Rates During Close-Coupled Gas Atomization Using Secondary Dendrite Arm Spacing Measurement. *Met. Mater. Trans B* **2013**, *44*, 992–999. [CrossRef]
8. Liu, T.; Leazer, J.D.; Menon, S.K.; Brewer, L.N. Microstructural Analysis of Gas Atomized Al-Cu Alloy Feedstock Powders for Cold Spray Deposition. *Surf. Coat. Technol.* **2018**, *350*, 621–632. [CrossRef]
9. Couper, M.J.; Singer, R.F. Rapidly Solidified Aluminium Alloys for Advanced Engineering Applications. *Process. Struct. Met. By Rapid Solidif.* **1987**, 273–282.
10. Sing, S.L.; Huang, S.; Goh, G.D.; Goh, G.L.; Tey, C.F.; Tan, J.H.K.; Yeong, W.Y. Emerging Metallic Systems for Additive Manufacturing: In-Situ Alloying and Multi-Metal Processing in Laser Powder Bed Fusion. *Prog. Mater. Sci.* **2021**, *119*, 100795. [CrossRef]
11. Fan, S.; He, B.; Liu, M. Effect of Pulse Current Density on Microstructure of Ti-6Al-4V Alloy by Laser Powder Bed Fusion. *Metals* **2022**, *12*, 1327. [CrossRef]
12. Jimenez, E.H.; Kreitcberg, A.; Moquin, E.; Brailovski, V. Influence of Post-Processing Conditions on the Microstructure, Static, and Fatigue Resistance of Laser Powder Bed Fused Ti-6Al-4V Components. *J. Manuf. Mater. Process.* **2022**, *6*, 85. [CrossRef]
13. Zheng, Z.; Peng, L.; Wang, D. Defect Analysis of 316 L Stainless Steel Prepared by LPBF Additive Manufacturing Processes. *Coatings* **2021**, *11*, 1562. [CrossRef]
14. Schmeiser, F.; Krohmer, E.; Wagner, C.; Schell, N.; Uhlmann, E.; Reimers, W. In Situ Microstructure Analysis of Inconel 625 during Laser Powder Bed Fusion. *J. Mater. Sci.* **2022**, *57*, 9663–9677. [CrossRef]
15. Murmey, P.; Nichul, U.; Chikode, M.; Hiwarkar, V. Effect of Post-Processing on Corrosion Behavior of LPBF Built Inconel 718 Alloy. *JOM* **2023**, *75*, 32–44. [CrossRef]
16. Vanzetti, M.; Virgillito, E.; Aversa, A.; Manfredi, D.; Bondioli, F.; Lombardi, M.; Fino, P. Short Heat Treatments for the F357 Aluminum Alloy Processed by Laser Powder Bed Fusion. *Materials* **2021**, *14*, 6157. [CrossRef]
17. Rometsch, P.A.; Zhu, Y.; Wu, X.; Huang, A. Review of High-Strength Aluminium Alloys for Additive Manufacturing by Laser Powder Bed Fusion. *Mater. Des.* **2022**, *219*, 110779. [CrossRef]
18. Bosio, F.; Manfredi, D.; Lombardi, M. Homogenization of an Al Alloy Processed by Laser Powder Bed Fusion In-Situ Alloying. *J. Alloys Compd.* **2022**, *904*, 164079. [CrossRef]
19. Martinez, R.; Todd, I.; Mumtaz, K. *In Situ* Alloying of Elemental Al-Cu12 Feedstock Using Selective Laser Melting. *Virtual Phys. Prototyp.* **2019**, *14*, 242–252. [CrossRef]
20. Bartkowiak, K.; Ullrich, S.; Frick, T.; Schmidt, M. New Developments of Laser Processing Aluminium Alloys via Additive Manufacturing Technique. *Phys. Procedia* **2011**, *12*, 393–401. [CrossRef]
21. Wang, P.; Deng, L.; Prashanth, K.G.; Pauly, S.; Eckert, J.; Scudino, S. Microstructure and Mechanical Properties of Al-Cu Alloys Fabricated by Selective Laser Melting of Powder Mixtures. *J. Alloys Compd.* **2018**, *735*, 2263–2266. [CrossRef]
22. Lombardo, S.; Rosso, M. Heat Treatments for Aluminum Alloys: When, Why and How. *Matls. Perf. Charact.* **2017**, *6*, 20170011. [CrossRef]
23. Chen, Z.; Zhao, Y.; Zhang, Z. Theoretical and Experimental Study of Precipitation and Coarsening Kinetics of Θ' Phase in Al–Cu Alloy. *Vacuum* **2021**, *189*, 110263. [CrossRef]
24. Bogno, A.-A.; Khatibi, P.D.; Henein, H.; Gandin, C.-A. Quantification of Primary Dendritic and Secondary Eutectic Nucleation Undercoolings in Rapidly Solidified Hypo-Eutectic Al-Cu Droplets. *Met. Mater. Trans. A* **2016**, *47*, 4606–4615. [CrossRef]
25. Bedel, M.; Reinhart, G.; Bogno, A.-A.; Gandin, C.-A.; Jacomet, S.; Boller, E.; Nguyen-Thi, H.; Henein, H. Characterization of Dendrite Morphologies in Rapidly Solidified Al–4.5 Wt.%Cu Droplets. *Acta Mater.* **2015**, *89*, 234–246. [CrossRef]
26. Bedel, M.; Reinhart, G.; Bogno, A.-A.; Nguyen-Thi, H.; Boller, E.; Gandin, C.-A.; Henein, H. Dendrite Growth Morphologies in Rapidly Solidified Al-4.5wt.%Cu Droplets. *IOP Conf. Ser. Mater. Sci. Eng.* **2016**, *117*, 012055. [CrossRef]
27. Heringer, R.; Gandin, C.-A.; Lesoult, G.; Henein, H. Atomized Droplet Solidification as an Equiaxed Growth Model. *Acta Mater.* **2006**, *54*, 4427–4440. [CrossRef]
28. Kim, K.; Bobel, A.; Baik, S.-I.; Walker, M.; Voorhees, P.W.; Olson, G.B. Enhanced Coarsening Resistance of Q-Phase in Aluminum Alloys by the Addition of Slow Diffusing Solutes. *Mater. Sci. Eng. A* **2018**, *735*, 318–323. [CrossRef]

29. Farkoosh, A.R.; Pekguleryuz, M. Enhanced Mechanical Properties of an Al–Si–Cu–Mg Alloy at 300 °C: Effects of Mg and the Q-Precipitate Phase. *Mater. Sci. Eng. A* **2015**, *621*, 277–286. [CrossRef]
30. Martin, A.; San Sebastian, M.; Gil, E.; Wang, C.Y.; Milenkovic, S.; Pérez-Prado, M.T.; Cepeda-Jiménez, C.M. Effect of the Heat Treatment on the Microstructure and Hardness Evolution of a AlSi10MgCu Alloy Designed for Laser Powder Bed Fusion. *Mater. Sci. Eng. A* **2021**, *819*, 141487. [CrossRef]
31. Bosio, F.; Lagalante, I.; Manfredi, D.; Lombardi, M. Bespoke Multi-Step Homogenization Heat-Treatment for a Laser Powder Bed Fused AlSi10Mg4Cu Alloy Synthesized via in-Situ Alloying. *Mater. Charact.* **2023**, *195*, 112506. [CrossRef]
32. Marinucci, F.; Aversa, A.; Manfredi, D.; Lombardi, M.; Fino, P. Evaluation of a Laboratory-Scale Gas-Atomized AlSi10Mg Powder and a Commercial-Grade Counterpart for Laser Powder Bed Fusion Processing. *Materials* **2022**, *15*, 7565. [CrossRef] [PubMed]
33. Vanzetti, M.; Pavel, M.J.; Perez, L.; Padovano, E.; Aversa, A.; Weaver, M.; Brewer, L.N.; Bondioli, F. Gas Atomized AlSi10Mg+Cu Powders for Metal Additive Manufacturing. EPMA Publications. [CrossRef]
34. Prasad, A.; Mosbah, S.; Henein, H.; Gandin, C.-A. A Solidification Model for Atomization. *ISIJ Int.* **2009**, *49*, 992–999. [CrossRef]
35. Doebelin, N.; Kleeberg, R. *Profex*: A Graphical User Interface for the Rietveld Refinement Program *BGMN*. *J. Appl. Crystallogr.* **2015**, *48*, 1573–1580. [CrossRef] [PubMed]
36. Zhang, Z.-H.; Xiong, B.-Q.; Zhu, B.-H.; Zuo, Y.-T. Stability of Supersaturated Solid Solution of Quenched Al–X (X = Zn, Mg, Cu) Binary Alloys. *Rare Met.* **2014**, *33*, 139–143. [CrossRef]
37. Albu, M.; Krisper, R.; Lammer, J.; Kothleitner, G.; Fiocchi, J.; Bassani, P. Microstructure Evolution during In-Situ Heating of AlSi10Mg Alloy Powders and Additive Manufactured Parts. *Addit. Manuf.* **2020**, *36*, 101605. [CrossRef]
38. Shabestari, S.G.; Moemeni, H. Effect of Copper and Solidification Conditions on the Microstructure and Mechanical Properties of Al–Si–Mg Alloys. *J. Mater. Process. Technol.* **2004**, *153–154*, 193–198. [CrossRef]
39. Almeida, B.A.; Ferro, M.C.; Ravanan, A.; Grave, P.M.F.; Wu, H.-Y.; Gao, M.-X.; Pan, Y.; Oliveira, F.J.; Lopes, A.B.; Vieira, J.M. Study of Multi-Carbide B_4C-SiC/(Al, Si) Reaction Infiltrated Composites by SEM with EBSD. *IOP Conf. Ser. Mater. Sci. Eng.* **2014**, *55*, 012001. [CrossRef]
40. Nafsin, N. Effects of Copper and Magnesium on Microstructure and Hardness of Al-Cu-Mg Alloys. *Int. J. Eng. Adv. Technol. (IJEAT)* **2013**, *2*, 533–536.
41. Martucci, A.; Bassini, E.; Lombardi, M. Effect of Cu Content on the PBF-LB/M Processing of the Promising Al-Si-Cu-Mg Composition. *Metals* **2023**, *13*, 1315. [CrossRef]